

# Quantifying mass-loss rate reduction and wind porosity using *Chandra* HETGS emission line profiles of $\zeta$ Puppis

David H. Cohen<sup>1</sup>, Maurice A. Leutenegger<sup>3</sup>, Asif ud-Doula<sup>1,2</sup>, Stanley P. Owocki<sup>2</sup>

## ABSTRACT

We explore the joint effects of mass-loss rate reduction and wind porosity on symmetrizing X-ray emission line profiles, using the *Chandra* grating spectrum (*Co-authors: we may add XMM data to the analysis*) of  $\zeta$  Puppis as a test case. We focus on three relatively high signal-to-noise, representative lines – Ne X at 12.13 Å, Fe XVII at 15.01 Å, and O VIII at 18.97 Å (*Co-authors: we can add more lines to the analysis*) – and show that when the data are of high enough quality, small values of wind optical depth,  $\tau_*$ , and porosity length,  $h$ , are preferred over porous models with larger optical depths. We quantitatively explore the trade-offs between  $\tau_*$  and  $h_\infty$  – the terminal velocity porosity length – in those cases where models with high porosity and high wind optical depth provide acceptable fits. We find that  $h_\infty \approx 5 R_*$  before the  $\tau_*$  values implied by the literature mass-loss rate can be accommodated. We also find that porosity has little effect on the line-profile fits for  $h_\infty \lesssim 1 R_*$ . *Co-authors: A sentence or two about introducing the non-isotropic porosity model in the context of the porosity length formalism, and the results of fits with this model.* By both examining the porosity length (*Co-authors: we haven't done this yet, and it may prove to be too problematic and/or not worth doing*) and by synthesizing line profiles from the output of two-dimensional numerical simulations of the wind instability, we show that physically realistic clumpy and porous wind structure does not have large enough porosity lengths to significantly affect the emergent X-ray line profile shapes. We also explore the overall level and wavelength dependence of the atomic opacity via detailed modeling and show that relatively flat opacities between 0.5 and 1 keV are easily obtained in a smooth wind.

*Subject headings:* line: profiles — stars: early-type — stars: mass loss — stars: winds, outflow — stars: individual ( $\zeta$  Pup) — X-rays: stars

---

<sup>1</sup>Swarthmore College Department of Physics and Astronomy, 500 College Ave., Swarthmore PA 19081

<sup>2</sup>Bartol Research Institute, University of Delaware, 217 Sharp Laboratory, Newark DE 19716

<sup>3</sup>Columbia University, Department of Physics and Columbia Astrophysics Laboratory, 550 W. 120<sup>th</sup> St., New York NY 10027

## 1. Introduction

X-ray emission line profiles provide very useful constraints on the physical properties of the hot, X-ray emitting plasma above the surfaces of O stars. The observed large line widths are evidence that the hot plasma resides in the stars’ radiation-driven winds, with the specific profile shapes providing information about the distribution of line-of-sight velocity in the hot plasma. Attenuation via continuum opacity in the cool, bulk wind is manifest as a blue-shifted line peak and a red-skewed asymmetry, because the red-shifted photons arise in the back hemisphere of the wind, and are therefore subject to more attenuation, passing through a larger wind column, than the blue-shifted photons emitted from the front hemisphere (MacFarlane et al. 1991; Owocki & Cohen 2001). Thus the observed profile shapes also provide information about the wind optical depth, which in turn jointly constrains the effective wind opacity and the spatial distribution of the X-ray emitting plasma.

The roughly ten O stars that have been observed with the *Chandra* and *XMM* gratings typically<sup>1</sup> show wind-broadening, but less of the asymmetry and skewness expected from the effects of wind attenuation. These results have generally been interpreted as evidence for smaller mass-loss rates, in accord with other, recent indications from the analysis of UV, FUV, H-alpha, and radio observations of O star winds (*refs to be inserted*). However, recent work describing the effects of porosity on X-ray line profiles suggest that porosity’s symmetrizing effects can explain what previously had been interpreted as reduced continuum opacity (and, ultimately, attributed to reduced mass-loss rates), though only by invoking very large inter-clump spacing (Oskinova, Feldmeier, & Hamann 2006). This raises two questions: (1) How do line-profile fits with and without porosity compare quantitatively? And (2) To the extent that porous models provide acceptable fits, are the large derived porosity lengths physically reasonable?

To address these two issues we first fit several of the stronger lines in the *Chandra* HETGS spectrum of  $\zeta$  Pup with a parameterized wind model that includes porosity effects. By doing this, we can address, quantitatively, how well porous models fit the data and what the joint constraints are on the parameters that describe porosity and wind optical depth. Specifically, we can determine the values of the porosity length (defined in §2.2) that are required to fit the data, assuming that the literature mass-loss rates are correct. We address the second issue above by analyzing two-dimensional radiation-hydrodynamics simulations of the line-driven instability. We analyze the wind structure produced in these simulations

---

<sup>1</sup>There are special exceptions –  $\tau$  Sco (which is a B0 star) and, to a lesser extent,  $\theta^1$  Ori C – with quite narrow, but still resolved ( $v_{HWHM} \approx 200 \text{ km s}^{-1}$ ), X-ray emission lines. These special cases seem to involve magnetic fields, if not dynamo activity.

both by characterizing the porosity length (*Co-authors: This hasn't been done yet*) and by synthesizing X-ray line profiles using the clumped structure from the simulations.

In §2 we describe the data and the basic, isotropic porosity model we use for the initial analysis. In §3 we present the fits to the data, with emphasis on the joint constraints on the wind optical depth and the porosity length, assuming isotropic porosity (*i.e.* spherical clumps). In §4 we introduce an extension of our basic model, which accounts for non-isotropic porosity in the context of the porosity-length formalism. This model is equivalent to the compressed shells, or “pancakes” that have already been used to describe the X-ray line profiles of several O stars (Oskinova, Feldmeier, & Hamann 2006). We also present fits to the  $\zeta$  Pup *Chandra* data using this new, non-isotropic model in this section. In §5 we analyze the numerical simulations of an O star wind in order to investigate the extent to which the porosity requirements derived from fitting data in the previous sections are realistic. In §6 we present detailed calculations of the wind opacity, which are needed to interpret the derived wind opacity values in terms of mass-loss rates, as well as to assess the implications of the apparent grayness of the effective opacity. We discuss the results and summarize the conclusions in §7.

## 2. The Data and the Model

### 2.1. The Data

In this paper, we report primarily on fits to the Fe XVII emission line at  $\lambda = 15.014$  Å in the *Chandra* HETGS spectrum of  $\zeta$  Pup (MEG  $m = \pm 1$  orders; the HEG spectrum has negligible flux in this line). *Co-authors: Again, note that we can expand the scope of the data involved – both to more lines in the Chandra spectrum (including HEG too, for lines with enough counts, though 15.01 and 18.97 do not have enough counts in the HEG to warrant inclusion of those data for those lines) and to the long XMM RGS spectrum of  $\zeta$  Pup.* This line is representative - Kramer, Cohen, & Owocki (2003) fit the profile with a spherically symmetric wind model with attenuation (Owocki & Cohen 2001), and found a best-fit  $\tau_* = 1.0$ . We also report on fits to two other strong lines in the MEG spectrum of  $\zeta$  Pup – the Lyman-alpha lines of neon and oxygen, at 12.13 Å and 18.97 Å, respectively. *Maurice: I can change the quoted wavelengths to the nearest mÅ, throughout the paper.*

Although this data set has been discussed and analyzed in several previous papers (Cassinelli et al. 2001; Kramer, Cohen, & Owocki 2003; Leutenegger et al. 2006), we re-reduced the data using recent versions of the CIAO software package (v. 3.3) and the CALDB calibration files (v. 3.2.2), starting from the level 1 events table. We saw nothing unusual

in the data. The grating spectra we extracted appear very similar, if not identical to, those reported by previous authors. The effective exposure time of the observation is 67,636 s, with a total of 17,448 counts in the MEG first order spectra (+1 and –1 combined).

## 2.2. The Model

Detailed numerical simulations of the line-driven instability (LDI), performed under the assumption of one-dimensional spherical symmetry due to computational constraints, show that thin compressed shells of wind material form quite easily in the wind above about half a stellar radius (Cooper & Owocki 1994; Feldmeier, Puls, & Pauldrach 1997). Rapidly accelerated, rarefied wind material slams into these slow moving, dense shells, producing shock-heated plasma at temperatures of several million degrees, and associated X-ray emission. It is reasonable to assume that the cold, compressed shells break up on some lateral scale, although this effect obviously cannot be produced in one-dimensional simulations<sup>2</sup>. The effects of such “fragmented shells” have been studied in a series of papers (Feldmeier, Oskinova, & Hamann 2003; Oskinova, Feldmeier, & Hamann 2004) and recently this model has been compared to *Chandra* spectra of several O stars (Oskinova, Feldmeier, & Hamann 2005, 2006).

A more general treatment of the effect of wind clumping and the associated porosity on X-ray line profiles demonstrated that the key parameter is the porosity length,  $h \equiv \ell/f$ , where  $\ell$  is the characteristic clump scale,  $f \equiv \ell^3/L^3$  is the volume filling factor of the clumps, and  $L$  is the inter-clump spacing (Owocki & Cohen 2006). The porosity length can be thought of as the photon mean free path as it traverses the interclump medium, at least for optically thick clumps. The key quantitative conclusion is that the porosity length must be of order the local radius,  $r$ , before X-ray line profiles can be significantly affected. This conclusion is consistent with the conclusions drawn by Oskinova, Feldmeier, & Hamann (2006) from the comparison of their more specialized model with data. One goal of the current paper is to put this result on a firm quantitative and statistical footing, via the use of real data and the statistical analysis of model fits with adjustable parameters.

The line-profile model we use is the standard Owocki & Cohen (2001) four-parameter ( $\tau_*$ ,  $u_{\max}(\equiv R_*/R_{\min})$ , normalization, and  $q$ ) model, modified for the effects of isotropic porosity, using the effective opacity treatment of Owocki & Cohen (2006), according to eq. (8) in that paper. However, rather than assuming that the porosity length is proportional

---

<sup>2</sup>The first two-dimensional simulations of the LDI do indeed show structures on a rather small scale, both laterally and radially (Dessart & Owocki 2003)

to the local radius, as  $h = h'r$ , we assume that the clumps follow the wind velocity law (taken to be  $\beta = 1$ ) – the so-called “stretch” porosity, or “beta” porosity, model (Owocki 2006). The local value of the porosity length thus scales as  $h = h_\infty(1 - R_*/r)$ . This radial distribution of porosity length is reasonable if the clumps are embedded in the wind and move with a similar velocity to law to that of the bulk wind. Fortunately, the expression for the effective optical depth is analytically integrable with the beta porosity law. *Co-authors: Should we lay out the mathematics here? Substituting the beta porosity law into equation 8 and deriving/showing the governing equation for the profile (analogous to equation 11 in Owocki & Cohen (2006) – from the beta/stretch version of equation 9 combined with equation 10)?* This parameterization also has the benefit of allowing for a direct comparison to the parameter,  $n_o$ , which Oskinova, Feldmeier, & Hamann (2006) use to characterize the frequency at which clumps are released at the base of the stellar wind.

### 2.3. The Fitting Procedure

This wind profile with porosity model is implemented as a custom model in *XSPEC* (v. 11.3.1). It has five parameters described above, with the two most relevant ones being the terminal porosity length,  $h_\infty$ , and the fiducial wind optical depth,  $\tau_*$ . The other three parameters are the normalization (photons  $\text{s}^{-1} \text{cm}^{-2}$ ),  $u_{\text{max}}$ , which parameterizes the onset radius of X-ray emission, and  $q$ , which is the power-law index for the assumed radial dependence of the X-ray emitting plasma’s filling factor. These last four parameters are identical to those used by Owocki & Cohen (2001). The effect of porosity on the line profiles is completely accounted for by the single new parameter,  $h_\infty$ . We performed all of the fitting in *XSPEC*, and included a continuum component in all model fitting. The continuum was forced to be flat, but the height of the continuum was allowed to be a free parameter. We typically included a continuum region on either side of the line that was about as large as the wavelength range covered by the line itself, although we occasionally excluded nearby wavelength regions if they were contaminated by emission from other lines. This was the case for the Fe XVII line at 15.014 Å, for which we fit data on the range  $14.85 \text{ \AA} < \lambda < 15.13 \text{ \AA}$ , which excludes the continuum on the red side of the line, as it is contaminated by the broadened emission of another Fe XVII line at 15.26 Å. Following this procedure, we had 110 bins in the combined  $m = \pm 1$  MEG spectra. We used the C statistic (Cash 1979) as the fit statistic for all the fitting described in this paper, as the small number of counts in the extreme wings and the continuum invalidate the  $\chi^2$  statistic and its assumption of Gaussian-distributed errors.

### 3. Fitting the Isotropic Porosity Model to the Data

The first fit we performed was the most general: all five parameters ( $h_\infty$ ,  $\tau_*$ ,  $u_{\max}$ , normalization, and  $q$ ) were free to vary, as was the normalization of the continuum. The best-fit model parameters are in good agreement with the results of Kramer, Cohen, & Owocki (2003), including  $\tau_* = 1.1$  (compare to their 1.0), and has the best-fit terminal porosity length value of  $h_\infty = 0.00$ . The best-fit parameters are summarized in Table 1 (quoted errors on the fit parameters are 68% confidence limits, throughout). The best-fit model is shown, superimposed on the data in Fig. 1. The fit is very good. In fact, the very low C statistic value implies a rejection probability of only 3%. This is determined from fitting an ensemble of Monte Carlo simulated datasets and comparing the C statistic from the fit to the data to the distribution of C statistics generated from the Monte Carlo simulations (via the *goodness* command in *XSPEC*).

*Co-authors: We should think about what it means that the fit is formally so good. Perhaps the model is more detailed or complex than it needs to be considering the quality (S/N) of the data. We could eliminate one or more of the free parameters. But we really have no a priori way to decide which ones are reasonable to eliminate (and what values we'd fix them at). In fact, if we were to eliminate one parameter, I would say the most reasonable thing would be to fix  $q = 0$ . However, this won't "improve" the Monte Carlo probabilities (i.e. they'll still be too good/low). And fixing  $q = 0$  would have implications for high- $\tau_*$  fits, as we will see below, where we show that the high- $\tau_*$  fits require  $q \approx 1$ . Maybe the thing to do is to start off this section fixing  $q = 0$ . Then we can show that high- $\tau_*, h_\infty$  fits are really quite bad, with the strong blue wing, as is seen in Fig. 4, that doesn't fit the data. And only at that point would we allow that  $q$  could be a free parameter. So, we'd show that in order to get decent fits with models with high porosity (but still not nearly as good as models without porosity) you have to "artificially" crank up  $q$ .*

Given this best-fit model, we can quantify the uncertainties on the derived model parameters via the usual “ $\Delta C$  statistic” method. This allows us to see how much larger than zero  $h_\infty$  can be before the model fit is significantly worse than the best-fit model. It will also enable us to see how much higher the derived  $\tau_*$  value can be. We show the joint constraints on  $\tau_*$  and  $h_\infty$  in Fig. 2. It can be seen from this figure that at the 68% confidence level,  $h_\infty$  can be almost as large as  $1.7 R_*$ . But interestingly, even if  $h_\infty$  is this large,  $\tau_*$  does not have to increase by very much ( $\tau_* \approx 3$  if  $h_\infty = 1.7 R_*$  compared to the  $\tau_* \approx 15$  expected from the literature  $\dot{M}$  and  $\kappa$  values<sup>3</sup>).

---

<sup>3</sup>*Co-authors: A somewhat detailed calculation of the wavelength-dependent atomic opacity in the wind is pending.*

Next, we look at a model with a high  $\tau_*$  value; something consistent with the literature mass-loss rate. Without a specific, detailed calculation of the X-ray opacity of the wind, we are guided by previously published opacities and related quantities for this and other stars’ winds. We choose  $\tau_* = 15$  as the value representative of a smooth wind and the literature mass-loss rate. *Co-authors: I will explicitly show this calculation – and the implicit assumption for the value of  $\kappa$  – when I get a chance.*

In Fig. 3 we show the best-fit model with  $\tau_*$  fixed at 15, and all the other parameters free. The best fit model has  $h_\infty = 5.5 R_*$ . The lower limit on  $h_\infty$  is  $4.5 R_*$ . So, a rather large value of the porosity length is required if the mass-loss rate is not reduced<sup>4</sup>. The model parameters of this fit are summarized in Table 2. Note that  $R_{\min}$  did not change very much, but  $q$  did. The best-fit value is  $q = 0.82$ . This high  $q$  value will de-emphasize the wings of the line by weighting the inner wind more. Note also that a bump or flattening out of the profile can be seen near line center in this model. The model systematically overpredicts the flux in this part of the profile. *Co-authors: It should be noted that the C statistic (like the chi-square statistic) is unaffected by correlations in the model-data deviations; by long runs of bins that all either over- or under-predict the level seen in the data. Some rank-order statistic (like the K-S statistic) might be more sensitive in this regard.*

Note that this model is significantly worse than the best-fit model shown in Fig. 1 – the C statistic is 98 compared to 86 (implying > 99% significance). *Co-authors: We will likely be refitting the data with a background spectrum included. This will not change the results but will change the raw values of the C statistic.* However, because the quality of the best fit is so good, the significantly worse fit still has a reasonable goodness of fit. So, although we cannot rule out this high- $\tau_*$ , high- $h_\infty$  model, the low- $\tau_*$ , low- $h_\infty$  model is preferred – with high statistical significance – over the high- $\tau_*$ , high- $h_\infty$  model. Because the high- $\tau_*$ , high- $h_\infty$  model requires a large increase in  $q$ , and because one might reasonably choose to fix  $q = 0$  in order to keep the number of free model parameters small, it is instructive to look at a high- $\tau_*$ , high- $h_\infty$  model with  $q = 0$ . The best-fit model with  $\tau_* = 15$  and  $q = 0$  fixed is shown in Fig. 4 and described in Table 3. Indeed this fit is significantly worse than the others we have shown. This seems to be due to an excess of emission on the blue wing, which is a universal characteristic of high- $\tau_*$ , high- $h_\infty$  models (and which is suppressed by larger  $q$  values, as large  $q$  gives extra weight to the inner, slow-moving portions of the wind).

---

<sup>4</sup>Oskinova, Feldmeier, & Hamann (2006) find a value of  $n_o = 2.6 \times 10^{-5} \text{ s}^{-1}$  for  $\zeta$  Pup. Using their values for  $v_\infty$  and  $R_*$ , this value of  $n_o$  corresponds to  $h_\infty = 6.4 R_*$ . *Co-authors: Note that this value is now  $1.7 \times 10^{-4}$  in the recently accepted version of (Oskinova, Feldmeier, & Hamann 2006), corresponding to  $h_\infty = 1 R_*$ . It is fixed, now, not fit. Should we also quote this original value from their submitted manuscript that represents their fit-by-eye?*

To assess the level of degeneracy among the model parameters, we compare three of the models we have discussed above, without convolving them with the instrumental response. This comparison is shown in Fig. 5. It can be seen from this figure that the models produce line profiles with quite similar, though not identical, morphologies. However, as we have just shown, the systematic differences in these morphologies can, in fact, be distinguished with data of the quality of the Fe XVII 15.014 Å line in the ζ Pup MEG spectrum.

Finally, the high value of  $h_\infty$  found in the high- $\tau_*$  ( $\tau_* = 15$ ) model may be partly due to the nature of the stretch model, as parameterized by  $h_\infty$ . So, we also fit a model that parameterizes the radial dependence of the porosity length as  $h = h'/r$ , which was the assumption used by Owocki & Cohen (2006). Indeed, we find when we do this that, again, a model without porosity is preferred to one with porosity. Furthermore, when we force  $\tau_* = 15$ , we find a high value of  $h'$ . Quantitatively, we find that  $h'$  must be between 1.0 and 1.5; so, roughly four times smaller than the corresponding  $h_\infty$ . This is sensible, as the inner, optically thick, portion of the wind is where porosity will have its largest effect. And in this region, the wind speed is several times below the terminal velocity, so to get the same porosity length in the inner wind,  $h'$  must be smaller than  $h_\infty$  by a factor of a few. Profiles calculated using these two different assumptions regarding the porosity-length distribution are shown in Fig. 6. *Co-authors: we could eliminate this discussion/paragraph completely; what do you think? I'm inclined to keep in this brief discussion because the  $h'$  model was used in Owocki & Cohen (2006), and the  $h_\infty$  parameterization was not discussed there at all.*

The results we have reported on here, for Fe XVII at 15.014 Å, are representative of what we find for other lines, though generally the uncertainties associated with fitting other lines in the *Chandra* spectrum are greater, as the signal-to-noise of the 15.014 Å line is relatively high. However, we performed a comparable suite of fits to the Ne X Ly $_\alpha$  line at 12.134 Å. Two of these fits – a global fit with all parameters free and one in which we fix  $\tau_* = 15$  – along with the confidence contours in the  $\tau_*$ - $h_\infty$  plane are shown in Fig. 7 and the fit parameters are listed in Table 4. While high- $\tau_*$ , high- $h_\infty$  models are excluded at the 90% confidence level for this line too, the fits they provide are not as bad as the comparable fits to the Fe XVII 15.014 Å line. We also did the same for the oxygen Ly $_\alpha$  line at 18.97 Å. This line has a lower signal-to-noise than the neon Ly $_\alpha$  line, and consequently the bounds that can be placed on the model parameters are less stringent. Here the high wind optical depth model cannot be ruled out at all, although as can be seen in Fig. 8, the same correlation between  $\tau_*$  and  $h_\infty$  is seen in the fits to this line too. *Co-authors: I haven't included a table for the fits to this line, because the model parameters are so poorly constrained. Also, should we state the wavelength range over which we fit the data along with the total number of bins, for these two lines, as we did for the Fe XVII line?*

## 4. Including Non-isotropic Porosity in Models of the X-ray Emission Line Profiles

*Co-authors: Should this be an appendix instead? I think we'll want to discuss fits of the non-isotropic model to the data and perhaps compare isotropic and non-isotropic models directly. So, at this point, I feel we should include this within the body of the paper.*

### 4.1. Extending the Model to Include Non-isotropic Porosity

*Co-authors: We will lay out some of the formalism in (Owocki 2006)...*

### 4.2. Fits to the *Chandra* Spectrum

*Co-authors: Maurice has incorporated this model into windprof and we will do a series of fits like those described in the previous section...*

## 5. Porosity Structure in Two-Dimensional Numerical Simulations of Line-Driven Winds

Now that we have information about the quantitative requirements for porosity to have a significant effect on X-ray line profiles, we are ready to assess the likelihood that real winds have such large porosity lengths. The simplest assumption is that the line-driven instability, which is thought to lead to the shock heating and X-ray production in the first place, is also responsible for generating the clumping that could lead to porosity. It is also possible, however, that other mechanisms – perhaps photospheric disturbances, causing propagating density enhancements in the wind which, when modulated by rotation, lead to discrete absorption components (DACs) and co-rotating interaction regions (CIRs); or perhaps magnetic fields seeding wind structure – dominate the clumping at larger spatial scales.

To address the clumpy and porous structure generated by the LDI, we have examined state-of-the-art, two-dimensional (2D) radiation hydrodynamics simulations, as described in Dessart & Owocki (2003). Multiple snapshots from the simulations described in that paper were mapped onto a three dimensional grid, in order to provide a realistic distribution of cold wind material. The X-ray emitting plasmas was assumed to be smoothly distributed above some minimum radius and to have an emissivity proportional to the ambient density squared.

This scenario closely mirrors the assumptions in the Owocki & Cohen (2001) model, with  $q = 0$ . Note that the 2D simulations are isothermal, so X-ray emission cannot be directly computed from them in a straightforward way. And in any case, the method we adopt here allows for a clearer comparison to the line profiles expected from a corresponding smooth wind.

*Co-authors - but especially Luc and Stan: I'm unclear about a couple of things – reading Luc's email of May 21, 2006 to Stan – the description of how the different phi-slices were or weren't populated is a bit confusing to me: 12 degree wide wedges... but only 9 of them? And then your statement about "not actually us(ing) different 2D hydro inputs in other phi angles" is not so clear to me, either. Sorry for being obtuse. Maybe a useful way to address my confusion would be for you, Luc (and/or Stan) to comment on/modify the text I've written above. Another question I have is how you determined the opacity of the wind material (or, of individual clumps). What did you use for the atomic opacity? OK, wait, I assume that you fiddled the opacity to give the three values of  $\tau_*$ . Is that correct? Finally, why do the solid lines in the figure look a little bumpy too?*

In Fig. 9 we show a series of line profiles calculated from the simulations, as described above. Each panel has a different onset radius of X-rays ( $R_o$ ) (*Co-authors: we need to use consistent notation:  $R_o$  or  $R_{\min}$ ?*) and shows line profiles for three values of wind optical depth ( $\tau_*$ ), calculated using the clumped wind structure from the simulations and also from a corresponding smooth wind. The profiles that include clumping show a low level of random noise, as would be expected from the numerical simulation generated structure, but show very little, if any, systematic effects on the overall shapes. Examining the simulation output itself (figure 1 in Dessart & Owocki (2003)), this is not surprising, as the clumpy structure is quite small scale, yielding porosity lengths that are significantly less than a stellar radius. Note that this is quite different than the larger interclump spacing seen in one-dimensional simulations (Feldmeier, Puls, & Pauldrach 1997), probably because in one dimension, clumps (shells, really) are prone to collide and merge whereas in higher-dimensional simulations the shell fragments, or clumps, are able to move past each other without interacting or interacting via shearing, rather than merging. It seems likely that instabilities (e.g. Rayleigh-Taylor) also cause larger structures to fragment on small lateral scales. Finally, note that the small lateral scales of wind clumps (as distinct from, e.g., CIRs) have been noted in other studies, both theoretical (Dessart & Owocki 2002) and observational (Lepine & Moffat 1999).

*Co-authors: To what extent is it (a) possible and (b) desirable to compute porosity lengths directly from these same – or similar – simulations? Identifying discrete clumps, assessing their length scales and assessing interclump spacings might not be so straightforward. We could, alternatively, eyeball the simulation outputs and qualitatively/semi-quantitatively*

*characterize these values.*

## 6. Wind Opacity

*Co-authors: I have started using Joe MacFarlane's Prismspect code to model ionization and opacity (using his ATBASE atomic structure models). I have yet to include x-ray photoionization in the models, among other things, but I think it's desirable to include this in this paper. Not only is it necessary to have opacities to connect  $\tau_*$  to mass-loss rates, but the wavelength-dependence of these opacities has also become an issue with the opacities shown by Oskinova, Feldmeier, & Hamann (2006) and their discussion of gray opacity pointing to optically thick clumping.*

## 7. Discussion and Conclusions

## REFERENCES

- Cash, W. 1979, ApJ, 228, 939
- Cassinelli, J. P., Miller, N. A., Waldron, W. L., MacFarlane, J. J., & Cohen, D. H. 2001, ApJ, 554, L55
- Cooper, R. G. & Owocki, S. P. 1994, Ap&SS, 221, 427
- Dessart, L. & Owocki, S. P. 2002, A&A, 383, 1113
- Dessart, L. & Owocki, S. P. 2003, A&A, 406, L1
- Feldmeier, A., Oskinova, L., & Hamann, W.-R. 2003, A&A, 403, 217
- Feldmeier, A., Puls, J., & Pauldrach, A. W. A. 1997, A&A, 322, 878
- Kramer, R. H., Cohen, D. H., & Owocki, S. P. 2003, ApJ, 592, 532
- Lepine, S. & Moffat, A. F. J. 1999, ApJ, 514, 909

- Leutenegger, M. A., Paerels, F. B. S., Kahn, S. M., & Cohen, D. H. 2006, ApJ, in press (astro-ph/0606370)
- MacFarlane, J. J., Cassinelli, J. P., Welsh, B. Y., Vedder, P. W., Vallergera, J. V., & Waldron, W. L. 1991, ApJ, 380, 564
- Oskinova, L., Feldmeier, A., & Hamann, W.-R. 2004, A&A, 422, 675
- Oskinova, L., Feldmeier, A., & Hamann, W.-R. 2005, in *The X-ray Universe*, El Escorial, Madrid, Spain (astro-ph/0511019)
- Oskinova, L., Feldmeier, A., & Hamann, W.-R. 2006, MNRAS, in press (astro-ph/0603286)
- Owocki, S. P. & Cohen, D. H. 2006, ApJ, in press (astro-ph/0602054)
- Owocki, S. P. 2006, porosity notes for L. Oskinova,  
(astro.swarthmore.edu/~cohen/projects/porosity/iso-vs-aniso-por.pdf)
- Owocki, S. P. & Cohen, D. H. 2001, ApJ, 559, 1108

Table 1. Fitted parameters for the best global model – all parameters free

parameter	value <sup>a</sup>
$q$	$-0.02^{+.13}_{-.02}$
$\tau_*$	$1.1^{+0.7}_{-.01}$
$h_\infty$	$0.00^{+1.7}_{-.00}$
$R_{\min}$	$1.53^{+.11}_{-.11}$
C	82.95
rej. prob. <sup>b</sup>	3%

<sup>a</sup>Uncertainties quoted here and in other tables are the 68% confidence limits on a given parameter, calculated using the  $\Delta C = 1$  criterion while letting all the other parameters vary freely.

<sup>b</sup>The rejection probability represents the percentage of Monte Carlo simulated datasets which gave a C statistic value lower than that produced by the actual data.

Table 2. Parameters for a model with  $\tau_* = 15$  – all other parameters, including  $h_\infty$ , free

parameter	value
$q$	$0.82^{+.88}_{-.42}$
$\tau_*$	15
$h_\infty$	$5.5^{+1.2}_{-1.0}$
$R_{\min}$	$1.73^{+.23}_{-.06}$
C	98.44
rej. prob.	10%

Table 3. Parameters for a model with  $\tau_* = 15$  and  $q = 0$  – all other parameters, including  $h_\infty$ , free

parameter	value
$q$	0
$\tau_*$	15
$h_\infty$	$6.7^{+0.9}_{-1.2}$
$R_{\min}$	$1.56^{+0.08}_{-0.07}$
C	102.44
rej. prob.	21%

Table 4. Parameters for a porosity model fit to the Ne X line at 12.134 Å: the right-most column lists the fit parameters for a model with  $\tau_*$  fixed at  $\tau_* = 15$

parameter	value (all parameters free)	value ( $\tau_* = 15$ )
$q$	$0.16^{+0.24}_{-0.19}$	$0.45^{+0.23}_{-0.15}$
$\tau_*$	$1.89^{+3.52}_{-0.38}$	15
$h_\infty$	$0.37^{+2.43}_{-0.34}$	$4.10^{+0.70}_{-0.50}$
$R_{\min}$	$1.48^{+0.12}_{-0.11}$	$1.62^{+0.10}_{-0.08}$
C	79.40	84.40
rej. prob.	14%	21%

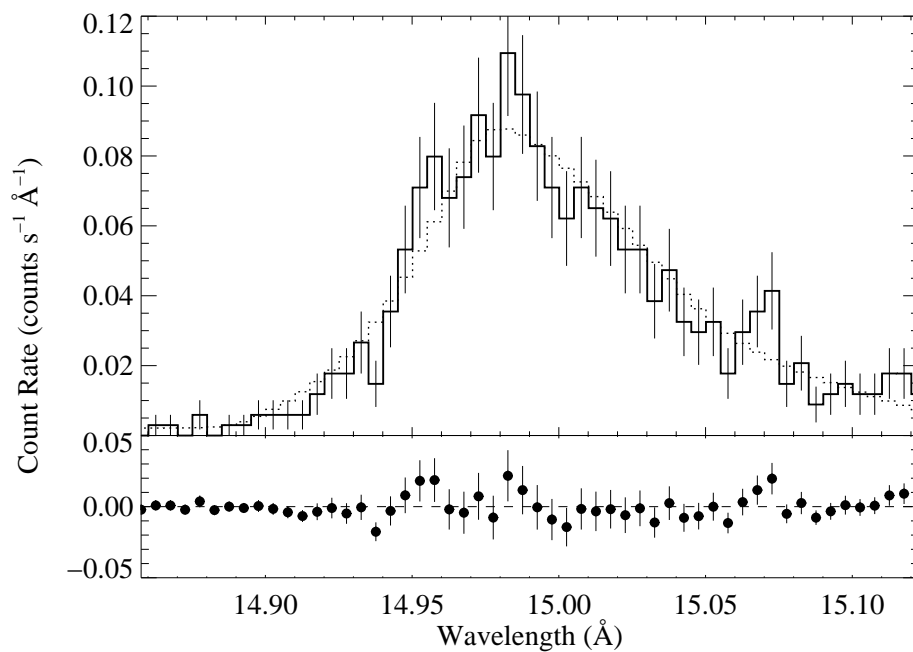


Fig. 1.— The global best-fit wind profile model for the Fe XVII line ( $\lambda_{\text{lab}} = 15.014 \text{ \AA}$ ) measured in the MEG first order (negative and positive orders co-added). In this model, the free parameters were  $h_{\infty}$ ,  $\tau_*$ ,  $u_{\text{max}}$ ,  $q$ , and the normalization of the line profile, as well as the normalization of the power-law continuum model (for which we fixed the power-law index at  $\alpha = 2$ ). The fit is formally good. (fexvii\_1501\_windprof\_best\_q\_thawed.ps)

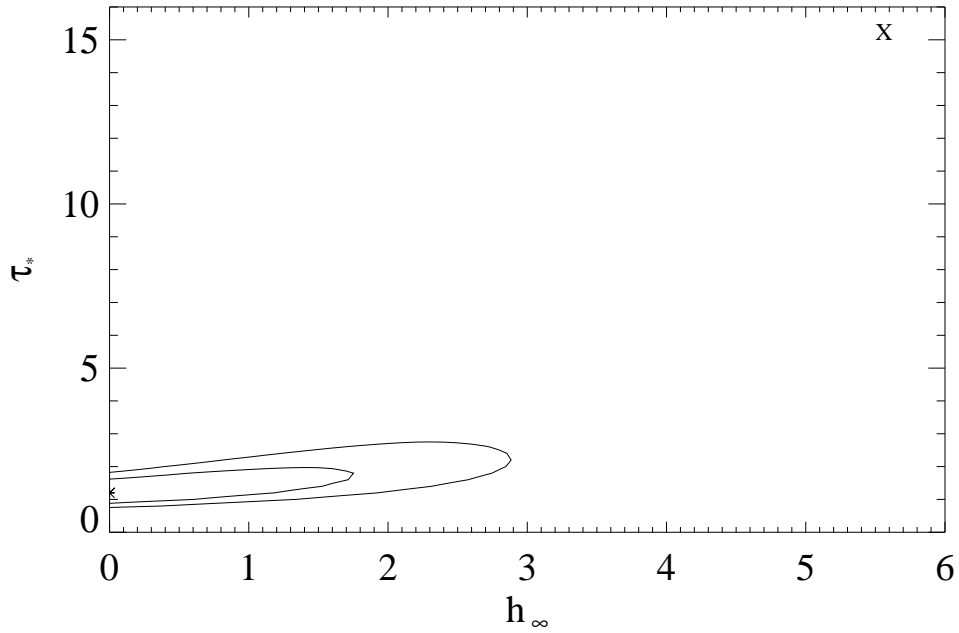


Fig. 2.— The 68% and 90% confidence regions for two parameters of interest ( $\Delta C = 2.30, 4.61$ ). The calculated grid is 20 by 20, and for each of the 400 models, the other parameters ( $q$ ,  $u_{\max}$ , normalization, and the normalization of the power-law continuum) were free to vary until a best-fit model for those values of  $\tau_*$  and  $h_\infty$  was found. The best-fit value on the grid is indicated with an asterisk (the fit shown in Fig. 1). The X indicates the best-fit  $h_\infty$  value for the fit where  $\tau_* = 15$  was fixed (the fit shown in Fig. 3). (fexvii\_1501\_hinf\_tau.ps)

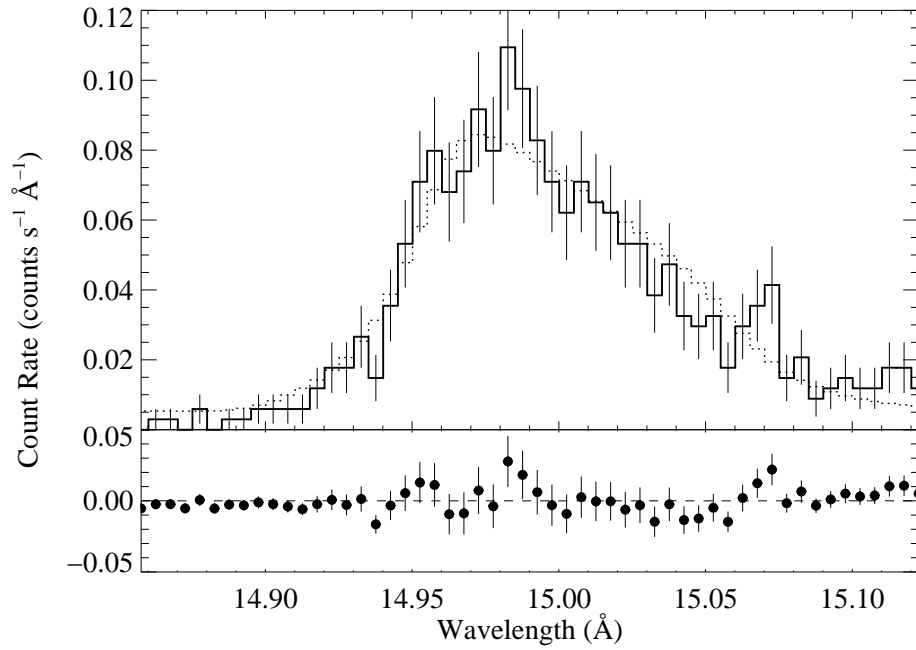


Fig. 3.— This fit has  $\tau_*$  fixed at 15, with all the other parameters being free. The terminal porosity length has a value of  $h_\infty = 5.5 R_*$ . The fit is significantly worse than the best-fit model shown in Fig. 1. The model seems to have trouble producing the observed profile shape on the red side of the line, especially. (fexvii\_1501\_windprof\_best\_tau\_15.ps)

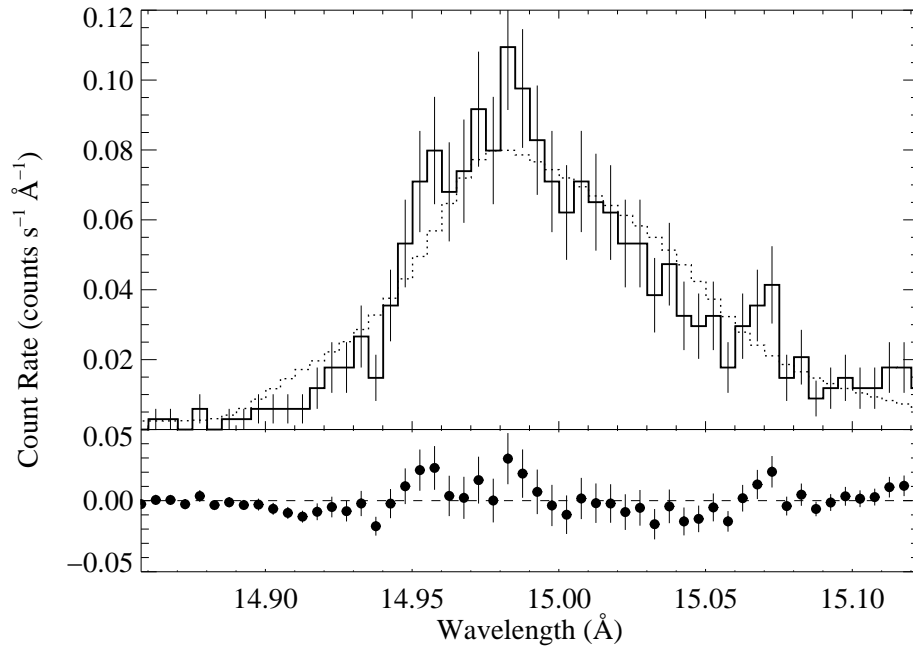


Fig. 4.— This fit has  $\tau_*$  fixed at 15 and  $q$  fixed at 0, with all the other parameters being free. Note the bump on the blue wing of the model in addition to the systematic over-prediction of flux on the red side of the profile, as is also seen in the fit shown in Fig. 3. The fit is significantly worse than the best-fit  $\tau_* = 15$ ,  $q$  free model shown in Fig. 3. (fexvii\_1501\_windprof\_best\_q\_fixed\_hinf\_thawed.ps)

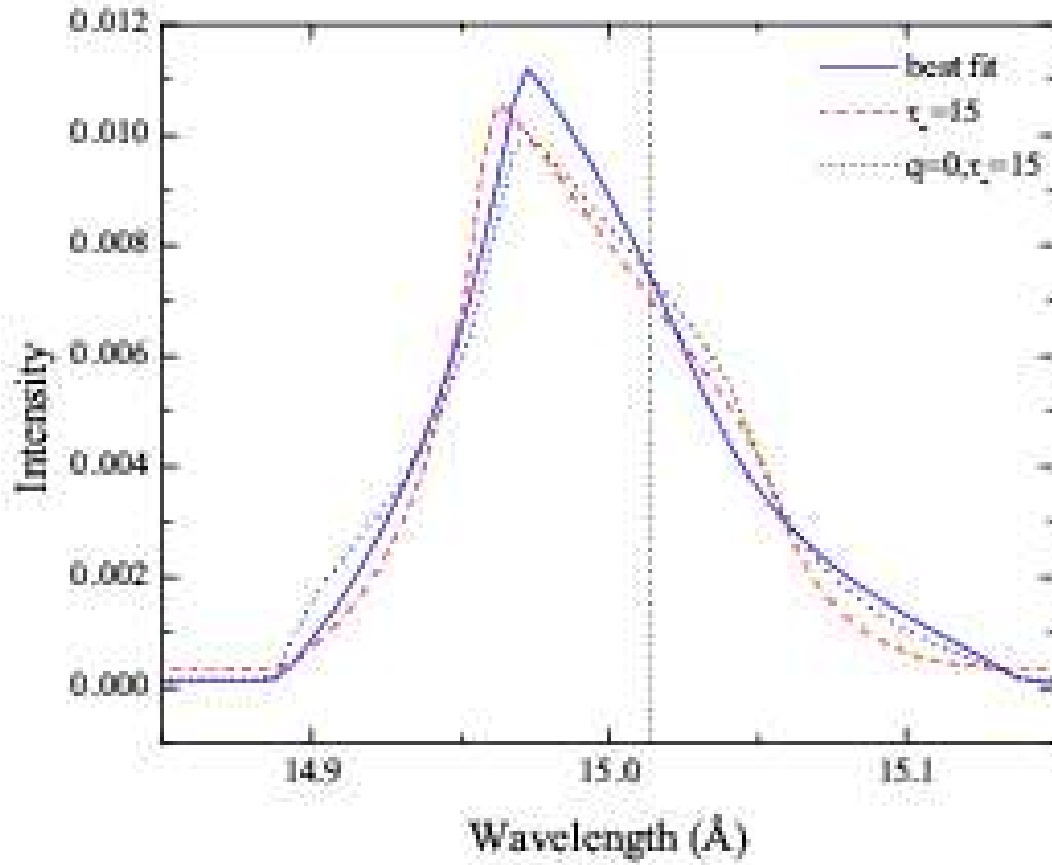


Fig. 5.— Three of the models we fit to the 15.014 Å line, shown with perfect resolution: the global best fit, the model with  $\tau_* = 15$ , and the model with  $\tau_* = 15$  and  $q = 0$ . *Co-authors: The image quality of this figure is fine when it's viewed in ghostview. Don't know what's going on with the embedding in LaTeX, but I'll get it figured out.* (best\_fit.eps)

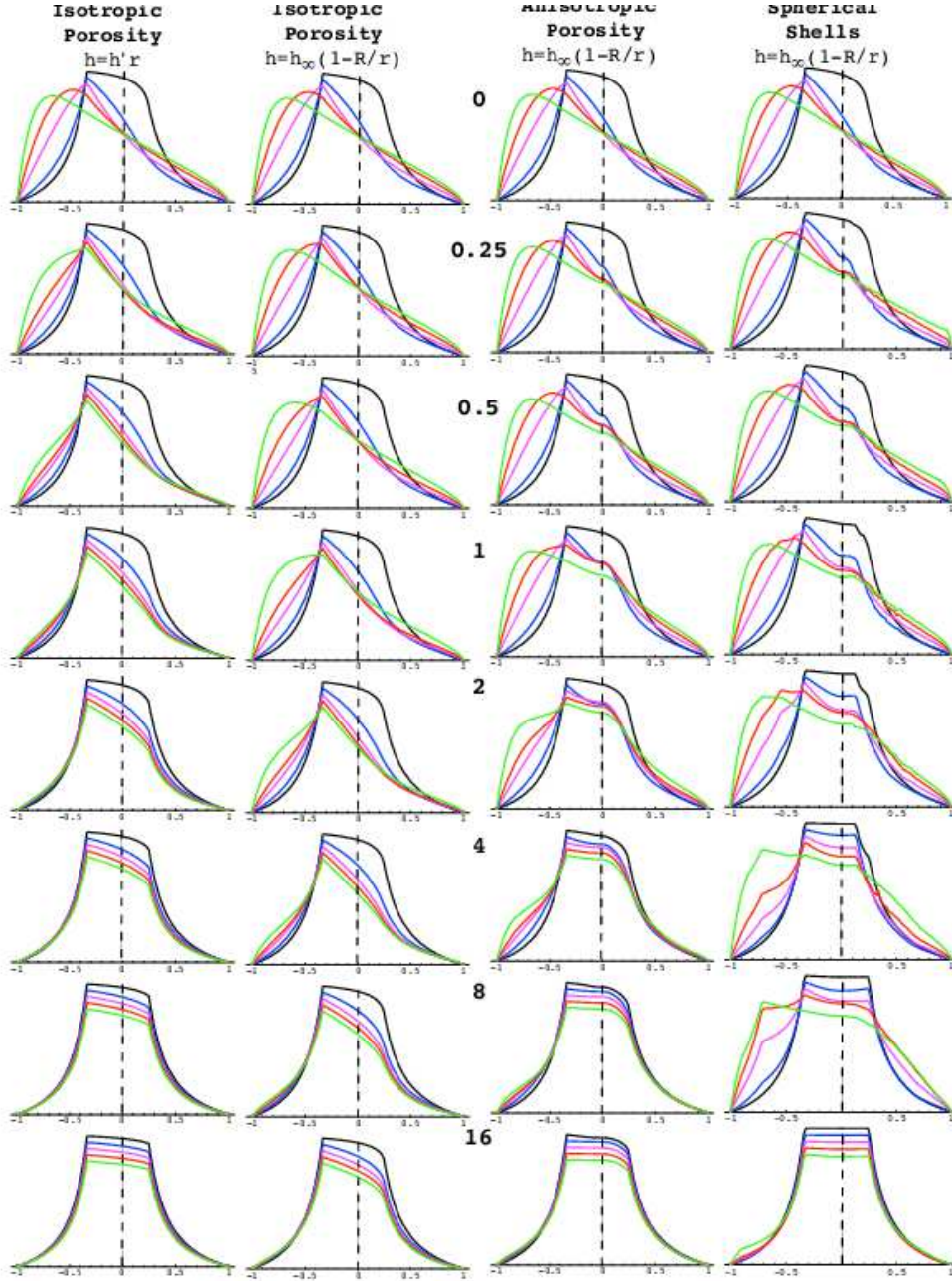


Fig. 6.— Suite of models comparing the linear treatment of porosity (left-most column) to the stretch (beta) treatment (second-from-left column) for a series of values of  $h'$  and  $h_\infty$ , respectively. In each panel, different values of  $\tau_*$  are shown. All models assume  $R_{\min} = 1.5R_*$  and  $q = 0$ . *Co-authors:* The third column shows non-isotropic porosity models, while the fourth column shows “shell” models, where each “clump” subtends  $4\pi$  steradians. Stan - or I - can remake this figure when we decide exactly what we want to show – maybe a reduced version of the second and third columns. (stan\_suite.eps)

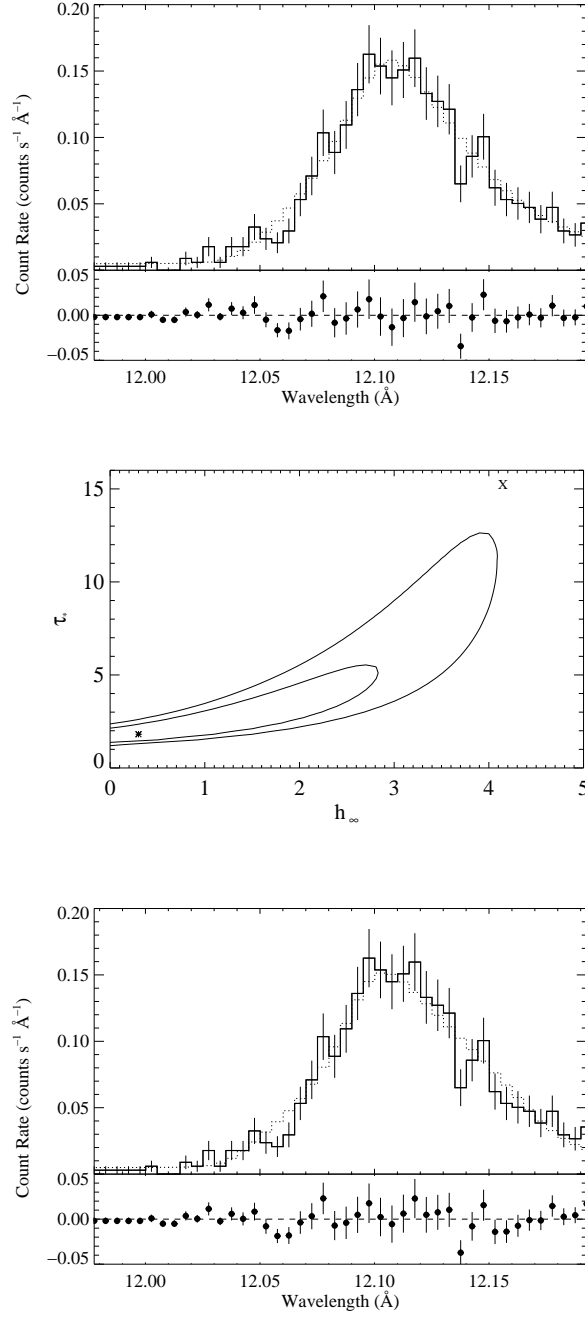


Fig. 7.— Best-fit porosity model – with all parameters free – fit to the Ne X Lyman-alpha line at 12.134 Å (top). We also show the 68% and 90% confidence limits for this fit (middle) and a fit to the same line with a porosity model for which we fixed  $\tau_* = 15$  (bottom). In the middle panel, the best global fit (shown in the top panel) is indicated by the asterisk, while the best-fit high optical depth model (shown in the bottom panel) is indicated by the X. (nex\_1213\_best\_fit.ps; NeX\_1213\_hinf\_tau.ps; nex\_1213\_best\_tau\_15.ps)

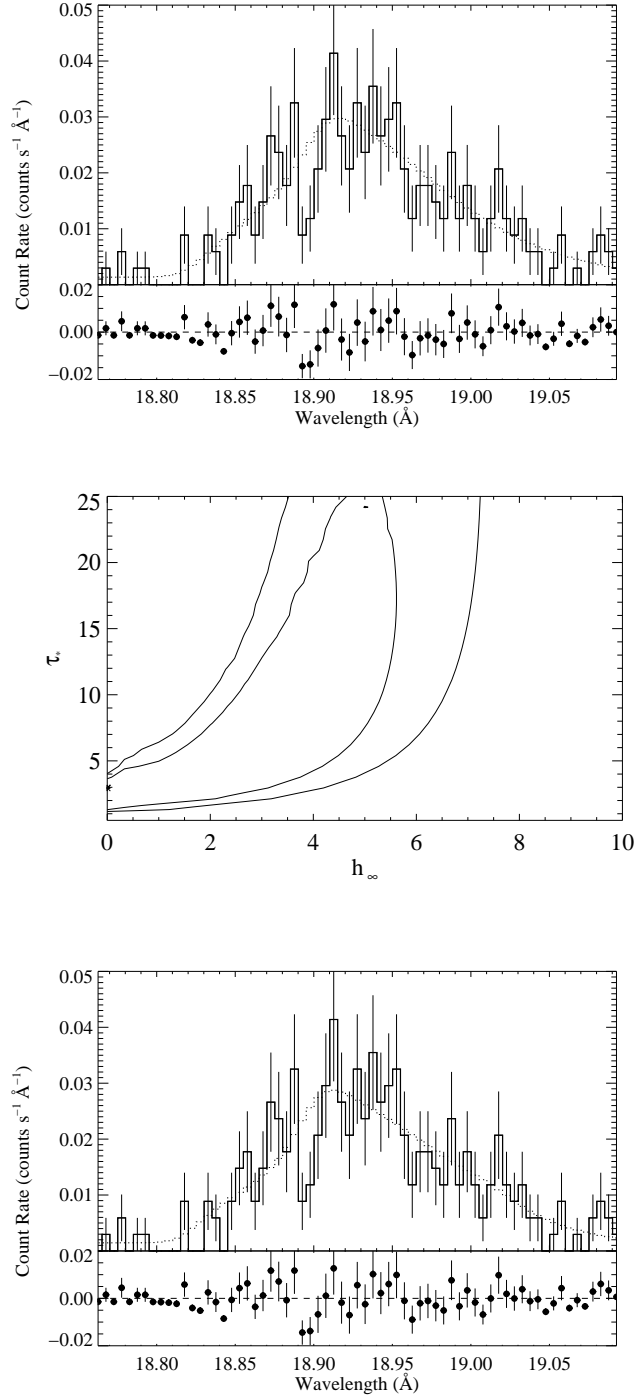


Fig. 8.— Best-fit porosity model – with all parameters free – fit to the Ne X Lyman-alpha line at 12.134 Å (top). We also show the 68% and 90% confidence limits for this fit (middle) and a fit to the same line with a porosity model for which we fixed  $\tau_* = 15$  (bottom). (nex\_1213\_best\_fit.ps; NeX\_1213\_hinf\_tau.ps; nex\_1213\_best\_tau\_15.ps)

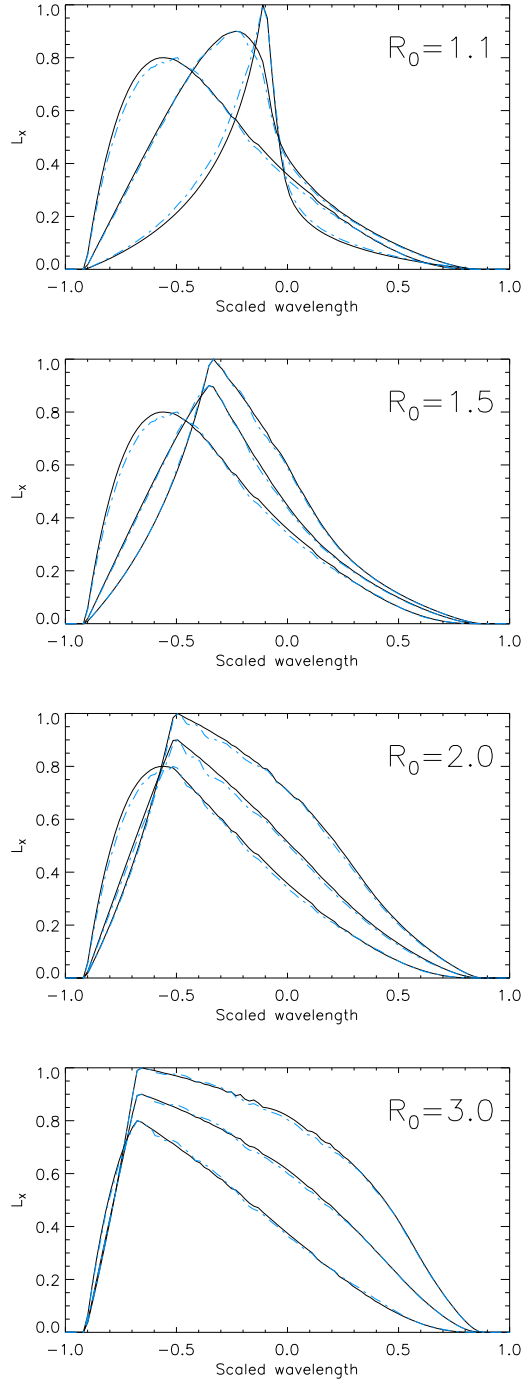


Fig. 9.— Line profiles calculated from the wind structure generated in 2D hydro simulations. The emission assumes an Owocki & Cohen (2001) model with  $q = 0$  and the onset radius,  $R_o = 1.1, 1.5, 2.0, 3.0 R_*$ , as indicated in each panel. Within each panel, we show profiles for three assumptions of the wind optical depth, given by  $\tau_* = 1, 2, 5$ . The numerically calculated profiles are indicated by the dashed lines, while the corresponding smooth-wind profiles are indicated by the solid lines. (xray\_porous\_q0.ps)